*J. Fluid Mech.* (1985), *vol.* 155, *pp.* 77–103
*Printed in Great Britain*



# Acoustic wave emitted by a vortex ring passing near the edge of a half-plane

By T. KAMBE,
Department of Physics, University of Tokyo, Bunkyo-ku, Tokyo 113, Japan

T. MINOTA AND Y. IKUSHIMA
Department of Applied Science, Kyushu University, Hakozaki, Fukuoka 812, Japan

(Received 3 July 1984)

Acoustic emission by vortex–edge interaction is investigated both theoretically and experimentally. The theory of vortex sound enables us to represent the far-field pressure in terms of the vortex motion near the half-plane edge. It is found that the pressure $p$ depends on the product of an angular factor representing directionality and a time factor representing wave profile. The pressure formula leads to the scaling law $p \propto U^{\frac{5}{2}}L^{-2}$ for the sound emitted by a vortex ring of velocity $U$, $L$ being the nearest distance of the vortex path to the edge. The sound intensity is proportional to $U^5$ and shows cardioid directionality pattern.

The vortex ring used in the experiment had radius about 4.7 mm and velocity ranging from 29 to 61 m/s. The above scaling law of the pressure and the cardioid directionality of the intensity were reproduced in the experiment with reasonable accuracy. Especially notable is the agreement between the predicted and observed wave profiles. The theoretical profile is determined by the $\frac{3}{2}$th time derivative of the volume flux (through the vortex ring) of a hypothetical potential flow around the edge.

## 1. Introduction

Theoretical formulation of the influence of solid boundaries on sound generation by unsteady flows was first made by Curle (1955), extending Lighthill's theory of aerodynamic sound (Lighthill 1952). Later, Ffowcs Williams & Hall (1970) and Crighton & Leppington (1970) considered noise generation by turbulent eddies in the vicinity of a sharp edge of the bounding surface, which is not included in Curle's theory. A dimensional analysis based on the idea that the velocity scale and lengthscale in the problem are given by those in the turbulence yields the law that the intensity of sound from free turbulence is proportional to the eighth power of the flow velocity, while that induced by the surface dipole of Curle's type is proportional to the sixth power. However, the sound generated by the edge–turbulence interaction is proportional in intensity to the fifth power of the flow velocity. Thus the wave field associated with the edge–turbulence interaction is more powerful at low Mach numbers than both Lighthill's quadrupole field and Curle's dipole field. In the analysis of Ffowcs Williams & Hall, the pressure of the aerodynamic sound is essentially described by the behaviour of a Green function of the linear wave equation. They point out that their conclusions rest upon the potential field singularity derived from the Green function.

We investigate here the wave emission by a circular vortex ring passing near the

edge of a half-plane (semi-infinite plane). The fifth-power law and emission directionality obtained in the turbulence–edge interaction are found to hold also in the vortex–edge interaction. The directivity diagram of the intensity takes the form of a cardioid curve in planes perpendicular to the edge. However, the pressure of the acoustic wave increases like $L^{-2}$ as the distance $L$ of the vortex path to the edge decreases, whereas in the turbulence–edge case it decreases like $L^{-\frac{3}{2}}$. This discrepancy is related to the difference that in the present vortex–edge case the timescale is given by $L/U$ and dependent on the *impact* distance $L$, $U$ being the vortex translation speed, while in the turbulence–edge analysis the timescale is assumed to be independent of $L$. One of the reasons for the use of a vortex ring in the present problem is that we can determine the temporal wave profile, owing to the simple geometry, and further can compare it with experimental observation. The potential flow around the edge plays a crucial role in this case, and the wave profile is found to be related to the $\frac{3}{2}$th time derivative of the *volume flux*, through the moving vortex ring, of the *hypothetical* steady potential flow around the edge.

The corresponding two-dimensional problem of acoustic emission from a vortex filament moving around a half-plane is considered by Crighton (1972), Howe (1975) and Möhring (1978) from various aspects. The cardioid intensity pattern as well as the wave profile was given by Crighton. Howe found that the rate at which the vortex traverses the streamlines of hypothetical potential flow around the edge determines the instantaneous intensity of the sound, whereas Möhring gave an explicit form of a vector function of the two-dimensional problem which is used in his vector Green-function formulation. Cannell & Ffowcs Williams (1973) investigated another two-dimensional radiation, from the motion of vortex filaments coupled to a semi-infinite duct, which also exhibits the edge effects.

In parallel with the mathematical analysis, we have conducted a corresponding experiment. The vortex ring used in the experiment had radius about 4.7 mm and velocity $U$ ranging from 29 to 61 m/s. It is interesting to find that the cardioid pattern is reproduced in the experiment. Furthermore, it is shown that the present theory can predict the observed wave profile with reasonable accuracy. We think this is one of the important results of the present work.

The cardioid pattern is also observed in the noise from a nozzle flow attached to one side of a large flat plate, which was measured by R. E. Hayden and is shown in figure 3.24 of Goldstein (1976).

In §2 the mathematical formulation of the vortex sound is summarized, giving a formula for the acoustic wave pressure emitted by vortex motion. The acoustic pressure is represented in terms of vorticity and Green function. Subsequently the Green function is given in the form of asymptotic series. This is derived from the exact form, which is known in the half-plane diffraction problem. Using this asymptotic expression we obtain an explicit expression for the acoustic pressure emitted from a vortex ring moving rectilinearly near the edge. This compact expression is given in §3. The present analysis is based on the inviscid equation of motion. General consideration of the viscosity effect is given in Kambe (1984) and Kambe & Mya Oo (1984). The experimental procedure is similar to that used in Kambe & Minota (1983) for the detection of the acoustic emission from head-on collision of two vortex rings. This is summarized in §4 together with a description of the setup. Data analysis and comparison with theory are described in §§5 and 6.

## 2. Mathematical formulation

### 2.1. *Pressure formula*

We consider a rigid half-plane (vanishingly thin) immersed in an unbounded inviscid fluid of uniform density $\rho_0$ at rest at infinity, where the sound speed is $c$. In order to make the discussion definite, we assume that (i) the flow is characterized by the representative scales of velocity $u$, length $l$ and time $l/u$, (ii) the characteristic Mach number $M = u/c$ is much less than unity, ensuring that a typical wavelength $\lambda$ of sound generated is much larger than the flow scale $l$, i.e. $\lambda = c(l/u) = l/M \gg l$, and (iii) non-zero vorticity is located well within a wavelength $\lambda$ from an origin taken on the edge of the half-plane. The conditions (ii) and (iii) will be called the compactness conditions below. Let us define the ratio

$$\epsilon = l/\lambda$$

as a smallness parameter in the present problem.

Sound emission from a localized flow at low Mach number is described by the inhomogeneous wave equation

$$\frac{1}{c^2}\frac{\partial^2}{\partial t^2}p - \nabla^2 p = \rho_0 \frac{\partial^2}{\partial x_i \partial x_j} v_i v_j, \tag{2.1}$$

(e.g. Lighthill 1952; Möhring 1978) where $p$ is the pressure and $\boldsymbol{v} = (v_i)$ the velocity. We seek a solution of this equation under an imposed boundary condition on the half-plane. In view of the assumption of low Mach number, the source flow can be described with sufficient accuracy by the equations of incompressible flow:

$$\frac{\partial}{\partial t}\boldsymbol{v} + (\boldsymbol{v}\cdot\nabla)\boldsymbol{v} = -\frac{1}{\rho_0}\nabla p, \quad \nabla\cdot\boldsymbol{v} = 0. \tag{2.2}$$

These are supplemented with the boundary condition of vanishing normal velocity at the rigid surface $S$.

We are here concerned with acoustic emission by vortex motion. The dynamics of the vorticity $\boldsymbol{\omega} = \operatorname{rot}\boldsymbol{v}$ is described by the equation,

$$\frac{\partial}{\partial t}\boldsymbol{\omega} + \operatorname{rot}(\boldsymbol{\omega}\times\boldsymbol{v}) = 0. \tag{2.3}$$

For incompressible motion, the source term on the right of (2.1) is rewritten as

$$\rho_0 \frac{\partial^2}{\partial x_i \partial x_j} v_i v_j = \rho_0 \operatorname{div}\boldsymbol{L}, \tag{2.4}$$

where

$$\boldsymbol{L} = (\boldsymbol{v}\cdot\nabla)\boldsymbol{v} = \boldsymbol{\omega}\times\boldsymbol{v} + \nabla\frac{v^2}{2}. \tag{2.5}$$

The inhomogeneous wave equation (2.1) with the right-hand side replaced by (2.4) is transformed into an integral form by using the Green function $G$ satisfying the equation

$$\left(\frac{1}{c^2}\frac{\partial^2}{\partial t^2} - \nabla^2\right) G(\boldsymbol{x}, \boldsymbol{y}; t) = \delta(\boldsymbol{x}-\boldsymbol{y})\,\delta(t), \tag{2.6}$$

together with the condition of vanishing normal derivative on the boundary surface $S$:

$$\frac{\partial G}{\partial n} = 0 \quad \text{on } S, \tag{2.7}$$

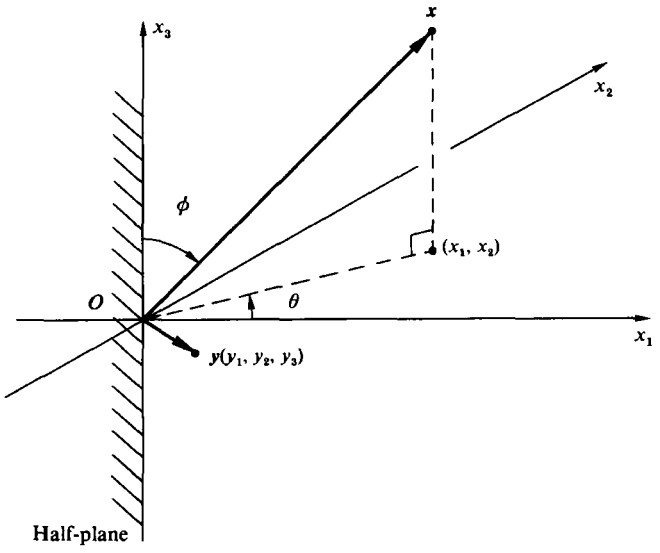


FIGURE 1. Definition sketch.

where $\partial/\partial n$ is the normal derivative. Performing partial integration once, we obtain

$$p(\boldsymbol{x},t) = -\rho_0 \int\int \nabla_y G(\boldsymbol{x},\boldsymbol{y};t-\tau)\cdot\boldsymbol{L}\,\mathrm{d}\boldsymbol{y}\,\mathrm{d}\tau, \tag{2.8}$$

where all the surface integrals vanish owing to the conditions (2.7), $\partial p/\partial n = 0$ and $\boldsymbol{L}\cdot\boldsymbol{n} = 0$ on $S$, $\boldsymbol{n}$ being the unit normal to $S$ and $\nabla_y$ the gradient operator with respect to the vector $\boldsymbol{y}$. According to Möhring's transformation procedure, which introduces a vector function $\boldsymbol{G}$ by the relation $\nabla_y G = \nabla_y \times \boldsymbol{G}$ with the condition $\boldsymbol{n}\times\boldsymbol{G} = 0$ for $\boldsymbol{y}$ on $S$, we find an alternative expression for the pressure:

$$p(\boldsymbol{x},t) = \rho_0 \frac{\partial}{\partial t}\int\int \boldsymbol{G}(\boldsymbol{x},\boldsymbol{y};t-\tau)\cdot\boldsymbol{\omega}(\boldsymbol{y},\tau)\,\mathrm{d}\boldsymbol{y}\,\mathrm{d}\tau. \tag{2.9}$$

The vector Green-function formulation is also developed by Obermeier (1979, 1980).

### 2.2. *Green function*

Our present problem is the study of acoustic emission by a vortex ring moving near the edge of a rigid half-plane $S$ which lies in

$$x_1 < 0, \quad x_2 = 0, \quad -\infty < x_3 < +\infty.$$

To this end we have to know the Green function $G(\boldsymbol{x},\boldsymbol{y};t)$ involved in the pressure formula (2.8). We are particularly interested in the value of the function $G(\boldsymbol{x},\boldsymbol{y};t)$ at a distant point $\boldsymbol{x} = (x_1,x_2,x_3)$ generated by a source at a point $\boldsymbol{y} = (y_1,y_2,y_3)$ (figure 1). We always consider the case where $\boldsymbol{y}$ is in the near field, well within a wavelength from the origin on the edge, and $\boldsymbol{x}$ in a distant wave region. By the reciprocal theorem for the wave equation (e.g. Landau & Lifshitz 1958), we may interchange the source and observation points, and solve for the field at a point $\boldsymbol{y}$ due to a source at a far-field point $\boldsymbol{x}$. Thus the problem reduces to the diffraction problem.

In order to find the Green function, it is convenient to use a series form, although a closed-form solution is known, as shown in Appendix A. This asymptotic analysis

leads to a mathematically simple formulation and physically transparent form of the law of the vortex sound. The compactness conditions (ii) and (iii) enable us to use the low-frequency Green function (Howe 1975), which is expressed by the first few terms of the asymptotic expansion series valid for small $kl = O(\epsilon)$, where $k$ is a wavenumber.

In Appendix A, Fourier expressions of the incident field $\hat{G}_0$ and the scattered field $\hat{G}_s$ are given in the series form, where the total field is given by $\hat{G}_0 + \hat{G}_s$. Using these and performing Fourier inversion by the formula (A 1), we obtain immediately the Green functions $G_0$ and $G_s$ in the series form

$$G_0(\boldsymbol{x}, \boldsymbol{y}; t) = \frac{1}{4\pi x}\left(\delta(t_r) + \frac{\boldsymbol{x}\cdot\boldsymbol{y}}{cx} \mathrm{D}_t\,\delta(t_r) + \frac{(\boldsymbol{x}\cdot\boldsymbol{y})^2}{2c^2x^2}\mathrm{D}_t^2\,\delta(t_r) + \ldots\right), \tag{2.10}$$

$$G_s(\boldsymbol{x}, \boldsymbol{y}; t) = G_{\frac{1}{2}} + G_1 + G_{\frac{3}{2}} + G_2 + \ldots, \tag{2.11}$$

where

$$G_m = \frac{A_m}{c^m}\,\Phi_m(\boldsymbol{X})\,\Phi_m(\boldsymbol{Y})\,x^{-m-1}\,\mathrm{D}_t^m\,\delta(t_*), \quad (m = \tfrac{1}{2}, 1, \ldots), \tag{2.12}$$

$$\mathrm{D}_t^m\,\delta(t) = \frac{1}{2\pi}\int_{-\infty}^{\infty} (-\mathrm{i}\omega)^m\,\mathrm{e}^{-\mathrm{i}\omega t}\,\mathrm{d}\omega, \quad \mathrm{D}_t = \frac{\partial}{\partial t}, \tag{2.13}$$

$$t_r = t - \frac{x}{c}, \quad t_* = t - \frac{1}{c}\,|\,\boldsymbol{x} - y_3\boldsymbol{k}\,|\,, \tag{2.14}$$

$$x = |\,\boldsymbol{x}\,|\,, \quad \boldsymbol{k} = (0, 0, 1),$$

and the variables $\boldsymbol{X} = (x_1, x_2)$ and $\boldsymbol{Y} = (y_1, y_2)$ are two-dimensional projections of $\boldsymbol{x}$ and $\boldsymbol{y}$. The constants $A_m$ $(m = \frac{1}{2}, 1, \ldots)$ are defined in (A 13) of Appendix A. The first few terms are used as the low-frequency Green function. It is to be noted that fractional derivatives appear in the terms $G_m$ with half-integer values of $m$.

If the Green function $G = G_0 + G_s$ is substituted in (2.8), we find that the contributions from the first two terms of (2.10) vanish and the contribution from $G_1$ vanishes too. This is because (i) the first term of $G_0$ does not include $\boldsymbol{y}$ and (ii) we have the vanishing integral,

$$\int L_i\,\mathrm{d}\boldsymbol{y} = \int_S v_i\,v_n\,\mathrm{d}S = 0,$$

from $G_1$ and the second term of $G_0$. Therefore the total Green function $G = G_0 + G_s$ may be well approximated by $G_{\frac{1}{2}}$:

$$\begin{aligned} G(\boldsymbol{x}, \boldsymbol{y}; t) &= A_{\frac{1}{2}}\,c^{-\frac{1}{2}}\Phi_{\frac{1}{2}}(\boldsymbol{X})\,\Phi_{\frac{1}{2}}(\boldsymbol{Y})\,x^{-\frac{3}{2}}\mathrm{D}_t^{\frac{1}{2}}\,\delta(t_*) \\ &= \frac{1}{(2\pi^3 c)^{\frac{1}{2}}}\,\frac{(\sin\phi)^{\frac{1}{2}}\sin\frac{1}{2}\theta}{x}\,\Phi_{\frac{1}{2}}(\boldsymbol{Y})\,\mathrm{D}_t^{\frac{1}{2}}\,\delta(t_*). \end{aligned} \tag{2.15}$$

The error incurred by ignoring $G_{\frac{3}{2}}$ and higher-order terms will be of order $\epsilon = l/\lambda$. It is remarkable that this form of the Green function is proportional to the velocity potential $\Phi_{\frac{1}{2}}(\boldsymbol{Y}) = Y^{\frac{1}{2}}\sin\frac{1}{2}\Theta$ of the irrotational flow around the edge, which contains the whole of the variation with $y_1$ and $y_2$.

With this form of the function $G$, we first note $\partial G/\partial y_3 = O(|\,G\,|/\lambda)$, which is smaller in order of magnitude than $\partial G/\partial y_1$ or $\partial G/\partial y_2$. Therefore $\nabla G$ is approximated with sufficient accuracy by the two-dimensional vector

$$\left(\frac{\partial}{\partial y_1}\Phi_{\frac{1}{2}}(\boldsymbol{Y}),\ \frac{\partial}{\partial y_2}\Phi_{\frac{1}{2}}(\boldsymbol{Y}),\ 0\right) A_{\frac{1}{2}}\,c^{-\frac{1}{2}}\Phi_{\frac{1}{2}}(\boldsymbol{X})\,x^{-\frac{3}{2}}\,\mathrm{D}_t^{\frac{1}{2}}\,\delta(t_*).$$

This approximation is consistent with the expression for $G$ given in (2.15). Introducing a stream function $\Psi(Y)$ corresponding to the potential flow $\Phi_{\frac{1}{2}}(Y)$ by the relation $\partial\Phi_{\frac{1}{2}}/\partial y_1 = \partial\Psi/\partial y_2$, $\partial\Phi_{\frac{1}{2}}/\partial y_2 = -\partial\Psi/\partial y_1$, we find that $\nabla G$ is also written as

$$\nabla G = \mathrm{rot}\,[\Psi(Y)\,k]\,A_{\frac{1}{2}}\,c^{-\frac{1}{2}}\Phi_{\frac{1}{2}}(X)\,x^{-\frac{3}{2}}\,\mathrm{D}_t^{\frac{1}{2}}\delta(t_*), \tag{2.16}$$

$$\Psi(Y) = -\,Y^{\frac{1}{2}}\cos\tfrac{1}{2}\Theta, \tag{2.17}$$

$$Y = |\,Y\,|, \quad \Theta = \tan^{-1}\frac{y_2}{y_1}.$$

Introducing (2.16) into (2.8), performing partial integration and using (2.3), we finally find the acoustic pressure as

$$p(x,t) = \rho_0\,\mathrm{D}_t\int\!\!\int \omega_3(y,\tau)\,F(x,y)\,\mathrm{D}_t^{\frac{1}{2}}\delta(t_*-\tau)\,\mathrm{d}y\,\mathrm{d}\tau$$

$$= \rho_0\,\mathrm{D}_t^{\frac{3}{2}}\int \omega_3(y,t_r)\,F(x,Y)\,\mathrm{d}y, \tag{2.18}$$

where $$F(x,Y) = A_{\frac{1}{2}}\frac{1}{(cx^3)^{\frac{1}{2}}}\,\Phi_{\frac{1}{2}}(X)\,\Psi(Y),$$

and $t_*$ is replaced by $t_r = t - x/c$ because of the compactness of the source. The far-field pressure depends only on the vorticity component parallel to the plate edge in the leading approximation. This final expression is equivalent to choosing the vector Green function as $G = (0,0,F)\,\mathrm{D}_t^{\frac{1}{2}}\delta(t_r)$ in (2.9).

## 3. A vortex ring moving near the edge

We consider a circular vortex ring of very thin core, whose centre is moving in a plane perpendicular to the $y_3$ axis. The intersection point of the plane and the $y_3$ axis is taken as the origin $O$. The nearest distance of the vortex centre path to the edge, i.e. to the origin $O$, is denoted by $L$. It is assumed below that $L$ is sufficiently larger than the vortex radius $a$. The normal to the plane of the vortex ring, taken in the direction of motion, lies in the $(y_1, y_2)$-plane and its direction is denoted as the $\xi$ axis. The $\eta$ axis is taken perpendicular to $\xi$ in the counterclockwise direction. The origin of the $(\xi, \eta, y_3)$-system is taken at the vortex centre $C$, its position being $(Y_1(t), Y_2(t))$ in the $(y_1, y_2)$-plane. The vorticity $\omega$ is assumed to be concentrated in a circle of radius $a$ with a very small cross-section, and the components of $\omega$ in the coordinate system $(\xi, \eta, y_3)$ are represented by

$$(0,\ -\Gamma\delta(\xi)\,\delta(\zeta-a)\sin\psi,\ \Gamma\delta(\xi)\,\delta(\zeta-a)\cos\psi),$$

where $\zeta = (\eta^2+y_3^2)^{\frac{1}{2}}$, and $\Gamma$ is the strength (circulation) of the vortex ring, $\psi$ the azimuthal angle of a point along the ring circumference from the $\eta$-axis, and $\zeta$ the radial coordinate in the $(\eta, y_3)$-plane. Substituting $\omega_3 = \Gamma\delta(\xi)\,\delta(\zeta-a)\cos\psi$ into (2.18) and integrating with respect to $\xi$ and $\zeta$, one obtains

$$p\left(x,\ t+\frac{x}{c}\right) = \rho_0\,\Gamma\,\mathrm{D}_t^{\frac{3}{2}}\int_0^{2\pi} F(\theta,\ \zeta=a,\ \xi=0;\ C(t))\,a\cos\psi\,\mathrm{d}\psi, \tag{3.1}$$

where the $x$-dependence of $F$ is omitted for simplicity, and $C(t)$ denotes the position of the vortex centre at the time $t$. In view of the condition $a/L \ll 1$, we approximate the function $F$ by the first two terms of the Taylor series,

$$F(\zeta=a,\ \xi=0;\ C) = F(C) + \frac{\partial}{\partial\eta}F(C)\,a\cos\psi,$$

since $F$ is independent of $y_3$. Then we have

$$\int_0^{2\pi} Fa\cos\psi\,\mathrm{d}\psi = \pi a^2\frac{\partial}{\partial\eta}F(C) = B\pi a^2 v_n(C), \tag{3.2}$$

where

$$\left.\begin{aligned} v_n &= \frac{\partial}{\partial\eta}\Psi(C) = \frac{\partial}{\partial\xi}\Phi_{\frac{1}{2}}(C), \\ B &= A_{\frac{1}{2}}c^{-\frac{1}{2}}x^{-\frac{1}{2}}\Phi_{\frac{1}{2}}(X) = \frac{1}{(2\pi^3 c)^{\frac{1}{2}}}\frac{\sin\frac{1}{2}\theta\,(\sin\phi)^{\frac{1}{2}}}{x}. \end{aligned}\right\} \tag{3.3}$$

The quantity $\pi a^2 v_n$ is the total volume flux of the hypothetical potential flow (around the edge) passing through the vortex ring. Introducing (3.2) and (3.3) into (3.1), we finally find the pressure formula

$$p\left(\boldsymbol{x}, t+\frac{x}{c}\right) = \frac{\rho_0\Gamma}{(2\pi^3 c)^{\frac{1}{2}}}\frac{\sin\frac{1}{2}\theta\,(\sin\phi)^{\frac{1}{2}}}{x}\,\mathrm{D}_t^{\frac{3}{2}}[\pi a^2 v_n(C)]. \tag{3.4}$$

Thus we have found that the pressure is proportional to $\sin\frac{1}{2}\theta\,(\sin\phi)^{\frac{1}{2}}$. This angular dependence is the same as that of a turbulent eddy in the vicinity of the half-plane, investigated by Ffowcs Williams & Hall (1970). Compared with their analysis of turbulent eddies, the present problem has an advantage enabling an explicit determination of the temporal profile of the pressure. This factor is represented by the time derivative, of the $\frac{3}{2}$th order, of the volume flux $\pi a^2 v_n$ through the ring. The flux varies as the vortex moves about (as its centre $C$ translates along its path). The derivative $\mathrm{D}_t^{\frac{3}{2}}$ is divided into $\mathrm{D}_t$ and $\mathrm{D}_t^{\frac{1}{2}}$, and the $\frac{1}{2}$th derivative has the definition:

$$\mathrm{D}_t^{\frac{1}{2}}g(t) = \frac{1}{2\pi}\int_{-\infty}^{\infty}(-\mathrm{i}\omega)^{\frac{1}{2}}\hat{g}(\omega)\,\mathrm{e}^{-\mathrm{i}\omega t}\,\mathrm{d}\omega = \int_{-\infty}^{t}\dot{g}(s)\frac{\mathrm{d}s}{[\pi(t-s)]^{\frac{1}{2}}} \tag{3.5}$$

(see e.g. Lighthill 1978, §1.4 for the last expression) where $(-\mathrm{i})^{\frac{1}{2}} = \mathrm{e}^{-\frac{1}{4}\mathrm{i}\pi}$. The dot represents differentiation with respect to the argument.

*Rectilinear vortex motion*

If the vortex path is sufficiently distant from the edge, the influence of the half-plane on it is small and the path is regarded as rectilinear (Appendix B). Suppose that the vortex translation velocity is a constant $U\boldsymbol{e}$, where $\boldsymbol{e}$ is a unit vector with components $(\cos\alpha, \sin\alpha)$ in the $(y_1, y_2)$-plane (figure 2). Then the first derivative of $v_n$ is

$$\mathrm{D}_t v_n = U\boldsymbol{e}\cdot\boldsymbol{\nabla}v_n = U(\boldsymbol{e}\cdot\boldsymbol{\nabla})^2\Phi_{\frac{1}{2}}(\boldsymbol{Y}), \tag{3.6}$$

since

$$v_n = \frac{\partial}{\partial\xi}\Phi_{\frac{1}{2}} = (\boldsymbol{e}\cdot\boldsymbol{\nabla})\Phi_{\frac{1}{2}}(\boldsymbol{Y})$$

is independent of time. Using $\Phi_{\frac{1}{2}}(\boldsymbol{Y}) = Y^{\frac{1}{2}}\sin\frac{1}{2}\Theta$, one finds

$$(\boldsymbol{e}\cdot\boldsymbol{\nabla})\Phi_{\frac{1}{2}} = -\tfrac{1}{2}Y^{-\frac{1}{2}}\sin(\tfrac{1}{2}\Theta-\alpha), \quad (\boldsymbol{e}\cdot\boldsymbol{\nabla})^2\Phi_{\frac{1}{2}} = \tfrac{1}{4}Y^{-\frac{3}{2}}\sin(\tfrac{3}{2}\Theta-2\alpha), \tag{3.7}$$

since $(\boldsymbol{e}\cdot\boldsymbol{\nabla})\Phi_{\frac{1}{2}} = \mathrm{Re}[\mathrm{e}^{\mathrm{i}\alpha}\,\mathrm{d}f/\mathrm{d}z]$ and so on where $f = \Phi_{\frac{1}{2}}(\boldsymbol{Y}) + \mathrm{i}\Psi(\boldsymbol{Y}) = -\mathrm{i}z^{\frac{1}{2}}$ and $z = y_1 + \mathrm{i}y_2 = Y\mathrm{e}^{\mathrm{i}\Theta}$. Choosing the time origin at the instant when the vortex is nearest to the edge with the distance $Y = L$, one can assign the vortex position $(Y\cos\Theta, Y\sin\Theta)$ at the time $t$ as

$$Y\cos\Theta = Ut\cos\alpha \pm L\sin\alpha, \quad Y\sin\Theta = Ut\sin\alpha \mp L\cos\alpha, \tag{3.8}$$

where the upper sign holds for $0 \leqslant \alpha \leqslant \pi$ and the lower for $0 \geqslant \alpha \geqslant -\pi$.

Normalizing all the lengths of the inner flow field by $L$ and the time by $L/U$, we obtain

$$\mathrm{D}_t^{\frac{3}{2}}[\pi a^2 v_n] = \tfrac{1}{4}\pi a^2 U^{\frac{1}{2}}L^{-2}\,\mathrm{D}_t^{\frac{1}{2}}g(t), \tag{3.9}$$

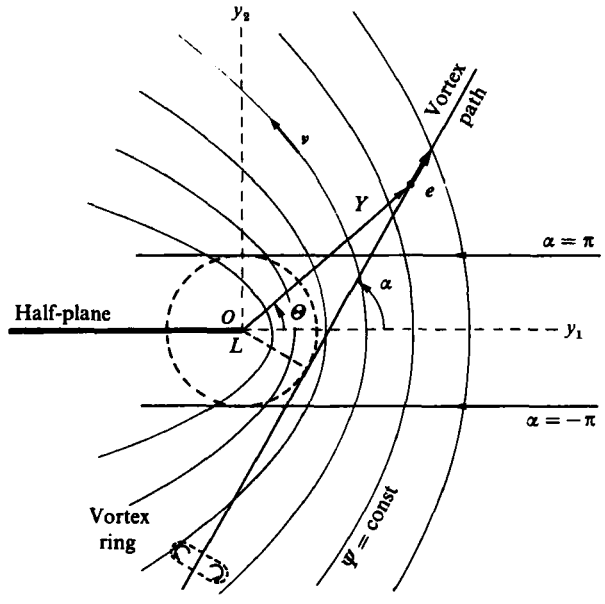


FIGURE 2. Vortex paths and the streamlines of the hypothetical potential flow around the edge.

where
$$g(t) = r^{-\frac{3}{2}} \sin(\tfrac{3}{2}\Theta - 2\alpha), \tag{3.10}$$

$$r = (t^2+1)^{\frac{1}{2}}, \quad \Theta = \tan^{-1}\left(\frac{t\tan\alpha \mp 1}{t \pm \tan\alpha}\right), \tag{3.11}$$

and the fractional derivative $\mathrm{D}_t^{\frac{1}{2}} g(t)$ is defined in (3.5) with the same notation $t$ used for the dimensionless time. Substituting (3.9) in (3.4), we obtain the acoustic pressure as

$$p\left(\boldsymbol{x}, t+\frac{x}{c}\right) = \frac{\rho_0 a^2 U^{\frac{3}{2}} \Gamma}{4(2\pi c)^{\frac{1}{2}} L^2} \frac{\sin\frac{1}{2}\theta\,(\sin\phi)^{\frac{1}{2}}}{x} \mathrm{D}_t^{\frac{1}{2}} g(t). \tag{3.12}$$

This shows that the pressure is proportional to

$$P_* = \rho_0 \frac{U^{\frac{3}{2}} \Gamma a^2}{c^{\frac{1}{2}} L^2 x}. \tag{3.13}$$

According to the well-known formula for the velocity $U$ of a vortex ring of core radius $\delta(\ll a)$,

$$U = \frac{\Gamma}{4\pi a} B, \quad \text{where } B = \ln\frac{8a}{\delta} - \frac{1}{4} \tag{3.14}$$

(Lamb 1932, §163), the strength $\Gamma$ is proportional to $Ua$ for a fixed value of the ratio $\delta/a$. Thus we find the pressure is proportional to

$$U^{\frac{1}{2}} L^{-2}. \tag{3.15}$$

The $U$-dependence $p \propto U^{\frac{1}{2}}$ is the same as that given by Ffowcs Williams & Hall (1970), who gave, however, a different $L$-dependence, $p \propto L^{-\frac{3}{2}}$. This discrepancy is ascribed to the fact that our vortex motion is scaled by the time $L/U$, whereas their case is independent of the impact distance $L$. The angular dependence is represented by the function

$$F(\theta, \phi) = \sin\tfrac{1}{2}\theta\,(\sin\phi)^{\frac{1}{2}}. \tag{3.16}$$

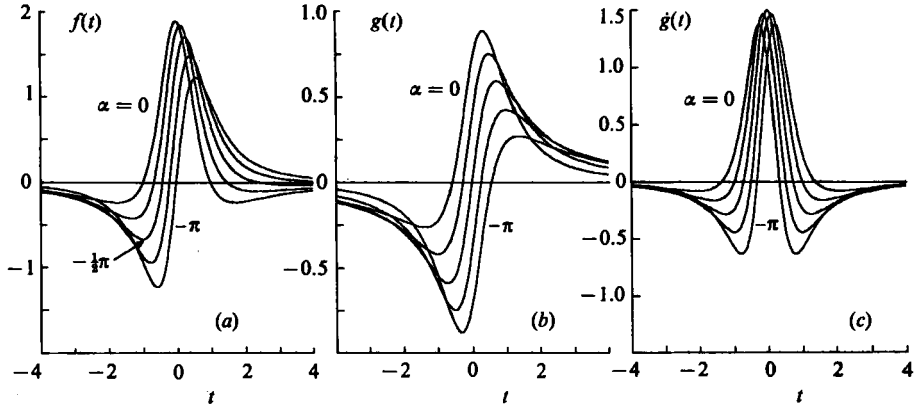


FIGURE 3. Three functions $f(t) = \mathrm{D}_t^{\frac{1}{2}} g(t)$, $g(t)$, and $\dot{g}(t)$ determining the wave profile for $\alpha = -\frac{1}{4}k\pi$ ($k = 0, 1, \ldots, 4$); $g(t) \propto \mathrm{D}_t[\pi a^2 v_n]$ is the rate of change of volume flux through the vortex ring.

The acoustic intensity is given by $p^2/\rho_0 c$, which is proportional to $U^5 L^{-4}$ and shows the directivity pattern of the cardioid curve $\sin^2 \frac{1}{2}\theta$ for fixed $\phi$, i.e. when received on the circle lying in the plane perpendicular to the edge with its centre at the edge.

The wave profile of the pressure is represented by

$$f(t) = \mathrm{D}_t^{\frac{1}{2}} g(t), \tag{3.17}$$

defined by (3.5) and (3.10). The three functions $f(t)$, $g(t)$ and $\dot{g}(t)$ were calculated for five values of $\alpha$ and shown in figure 3. It is seen that the curve $f(t)$ shows intermediate behaviour between that of $g(t)$ and $\dot{g}(t)$. Note that the $f$-curve of $\alpha = 0$ is symmetric with respect to the central point of the peak, while the curve of $\alpha = -\pi$ is anti-symmetric. The $f$-curves of positive $\alpha$ are obtained by taking inversion of those of $|-\alpha|$ with respect to the horizontal line $f = 0$.

## 4. Experimental setup and procedure

In order to detect the acoustic wave radiated by a vortex ring passing by a half-plane edge, one must have a device capable of producing a high-speed vortex and a system of apparatus that processes the acoustic signal received by the microphones. The device and apparatus are essentially the same as those used in the experiment to detect the acoustic radiation by head-on collision of two vortex rings (Kambe & Minota 1983). Figure 4 shows the experimental configuration, and figure 5 is a block diagram illustrating the data processing.

The vortex ring is produced by means of a shock tube. A shock wave generated in the tube is transmitted through a pipe to a straight nozzle in an anechoic chamber of inner size 1.8 m on all sides and emerges out of its circular open end of diameter $D = 6$ mm to the air at room condition. A jet pulse following the shock wave develops into a vortex ring of radius $a \approx 4.7$ mm, which moves forward with its self-induced velocity $U$ (29 m/s $\lesssim U \lesssim$ 61 m/s). Hence the Reynolds number $Re$ referred to the radius $a$ and the vortex speed $U$, i.e. $Re = aU/\nu$, ranges from $9.1 \times 10^3$ to $1.9 \times 10^4$. A large flat plate with a sharp edge is placed near the vortex path with a nearest distance $L$. The vortex ring passes by the edge without being broken as long as $L$ is greater than the ring radius $a$. The circular form of the ring is almost unchanged during the motion except for the paths with $L$ very near $a$. (This was observed in

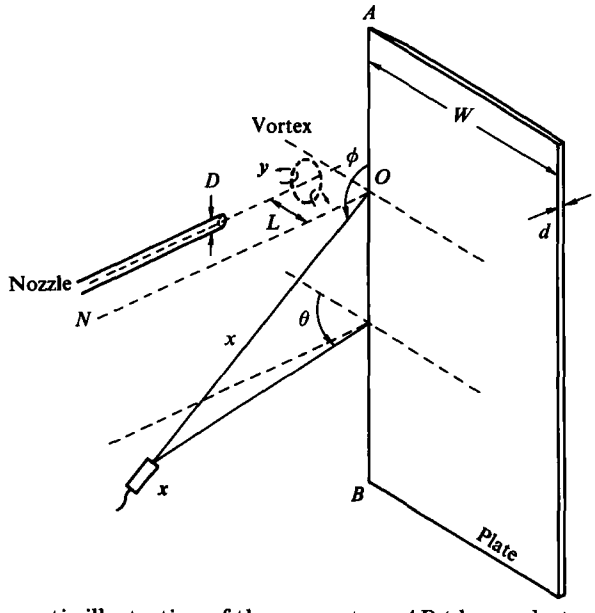


FIGURE 4. Schematic illustration of the apparatus: $AB$ (sharp edge) = 1.77 m, $W$ = 1.0 m, $d$ = 5 mm, $D$ (inner diameter) = 6 mm, vortex radius $\approx$ 4.7 mm.

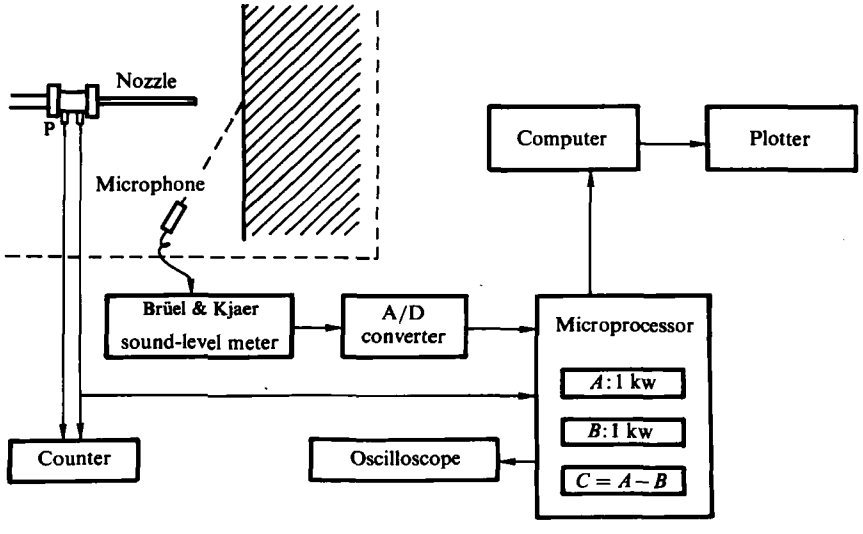


FIGURE 5. Block diagram showing data-processing system, P: pressure transducers.

a preliminary experiment with flow visualization at lower Reynolds numbers.) The nozzle is set in the plane perpendicular to the edge line. The plate had width $W$ = 1.0 m and the edge side had $AB$ = 1.77 m and thickness $d$ = 5 mm (the edge $AB$ being sharpened).

The relative position of the vortex from the nozzle is observed in the presence of the plate edge as a function of time. In figure 6 the distance $z$ (mm) of the vortex centre from the nozzle end is plotted against the time $T$ (μs) when the vortex moves perpendicularly to the plate (i.e. $\alpha = -\frac{1}{2}\pi$), the time origin being fixed as described

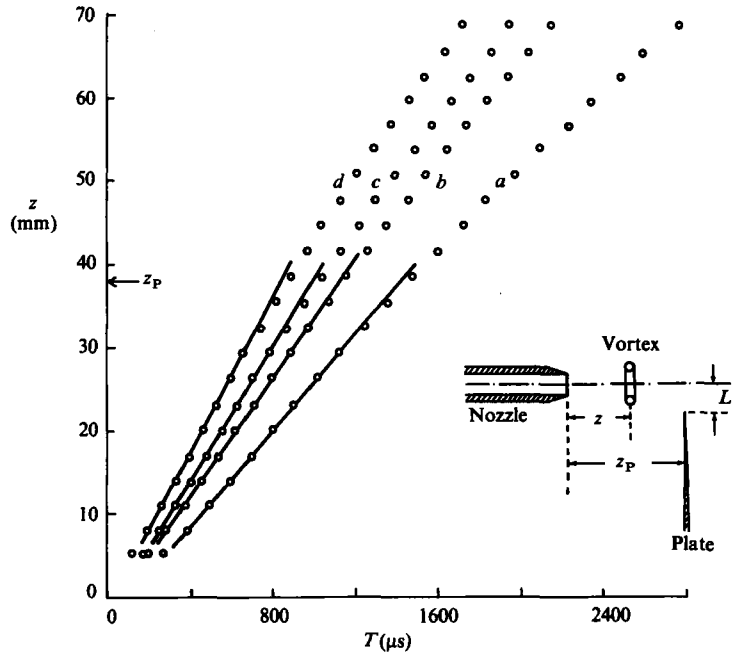


FIGURE 6. Vortex position $z$ from the nozzle end versus time $T$ for four cases of vortex motion in the presence of the edge plate with a fixed $z_P = 38$ mm, where the impact distance $L$ is 9.6 mm for (*a*), (*b*) and 9.7 mm for (*c*), (*d*). The solid tangent lines to the experimental plot of open circles correspond to the vortex speed $U$ of (*a*) 29.0, (*b*) 35.8, (*c*) 40.4 and (*d*) 46.3 m/s.

below. The observation is made for two values of the *impact* distance $L$ with $z_P = 38$ mm where $z_P$ is the distance between the nozzle end and the nearest point of the vortex path to the plate edge.

The acoustic wave emitted by the vortex–edge interaction is received with four microphones of diameter $\frac{1}{2}$ in. (Brüel & Kjaer type 4165). They are placed in the far field at distances $x = |\boldsymbol{x}|$ about 620 mm from the origin $O$ with different angles in the anechoic chamber. The microphone position is assigned by the angles $\theta$ and $\phi$ as shown in figure 4. The recording of the signal and its data-processing are performed by means of sound-level meters (Brüel & Kjaer type 2209), an A/D converter, a microprocessor, an electronic counter with a clock, a plotter and a computer.

The test procedures are as follows: (i) starting a shock wave to make a vortex ring at the nozzle exit; (ii) recording the sound waves received by the far-field microphones; and (iii) extracting the acoustic signals related to the vortex–edge interaction by eliminating irrelevant noise. The extraction procedure consists of four steps, which are now described.

First, the recording of the microphone signal is triggered by the shock signal from one of the two pressure transducers mounted at the junction between the nozzle and the pipe. The raw acoustic signal, including not only the required sound but unavoidable noise associated with the shock wave, is stored in a microprocessor in the form of a digital data set of 1000 words, denoted by $A$. An example of such an acoustic pressure signal (for the case $\alpha = \pi$), received at $\theta = 140°$ and $\phi = 90°$, is shown in figure 7 (*a*), where the vortex speed $U$ was 30.2 m/s. The sampling time was 3 μs; hence the total timespan is 3000 μs (= 3 ms) as shown in the figure. The time origin is fixed by the trigger-signal from the second pressure transducer with delay 1900 μs.

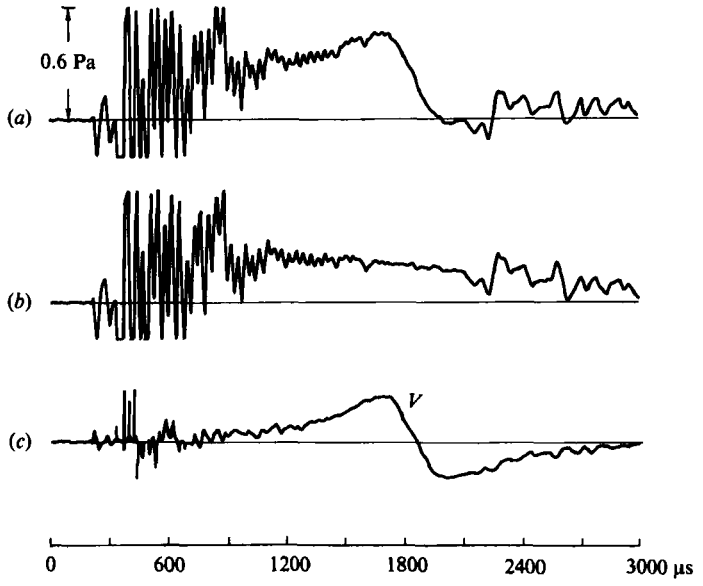


FIGURE 7. Acoustic signal obtained at $x = 624$ mm, $\theta = 140°$ and $\phi = 90°$ for the vortex motion $U = 30.2$ m/s, $L = 10.0$ mm and $\alpha = \pi$. (*a*) Data $A$ including the vortex-edge sound, (*b*) data $B$ without the vortex-edge sound, and (*c*) data $C\ (= A - B)$. The sampling time is 3 μs, and $A$, $B$ and $C$ are each 1000 words.

In order to extract the required signal from the data $A$, a second experiment is carried out to obtain the signal of noise only, not including the vortex–edge sound. A thin obstructing rod is placed just in front of the exit of the nozzle, where a vortex ring is supposed to form by the shock impulse. Motion of the vortex just formed is obstructed by the rod and the vortex is broken down immediately after its formation. Therefore, the signal of the vortex–edge sound does not appear at the time position where the data set $A$ includes it. The received pressure signal is also stored as a digital data set of another 1000 words, denoted by $B$. Its trace is shown in figure 7(*b*), with the same conditions as in the signal (*a*) except for the effect of the thin rod. However, the signal (*b*) possibly contains the waves generated by the interaction of the vortex with the rod which should appear earlier than the vortex–edge sound. Hence both signals are separated on the time axis.

In the third step we subtract the set of data $B$ from the data $A$ word by word. The trace of the data denoted by $C\ (= A - B)$ is shown in figure 7(*c*). The wave $V$ seen in the signal (*c*) is considered to be the acoustic pressure emitted by the vortex–edge interaction. The signal thus obtained still contains random fluctuation noise. Therefore the fourth step is to take an ensemble average over ten such sets of data, denoted by $\langle\ \rangle$. The final data represent an average profile of the vortex–edge sound received at $\theta = 140°$ and $\phi = 90°$. The acoustic pressures at various angular positions have been also measured with a fixed vortex speed.

In §5 we consider only the average waves $\langle V \rangle$, obtained for various conditions of $L$, $U$ and $\alpha$, and examine whether they have the properties predicted by the formulae (3.15)–(3.17). The data analysis that follows is based on the vortex radius $a$ and the translation speed $U$. Hence the time is scaled by $a/U$. We consider below three cases of vortex motion corresponding to $\alpha = -\frac{1}{2}\pi$, $\pi$ and $-\pi$.

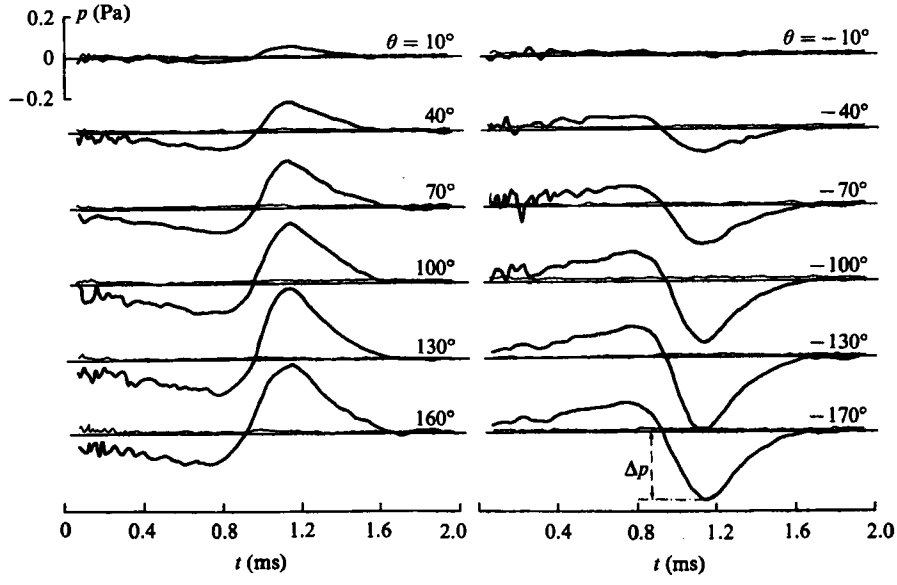


FIGURE 8. Average profiles (bold lines) of the acoustic pressure measured at twelve angular positions $\theta$ ($\phi = 90°$, $x = 634$ mm) for $U = 30.4$ m/s, $\alpha = -\frac{1}{2}\pi$ and $L = 9.6$ mm. Absolute scales are shown. The light curves denote r.m.s. error of the average curve at each time point.

## 5. Vortex motion with $\alpha = -\frac{1}{2}\pi$

### 5.1. *Directivity*

In this case the vortex moves perpendicularly to the half-plane and passes by its edge. In order to see whether the observed waves obey the theoretical directivity (3.16), we first show the profiles detected at various angles $\theta$ in the plane $\phi = 90°$, and then afterwards examine the $\phi$-dependence for fixed $\theta$.

Figure 8 shows the average profiles (bold lines) of the acoustic pressure at every $\pm 30°$ of angular position of $\theta$ from $\theta = \pm 10°$, with $U = 30.4$ m/s, $L = 9.6$ mm, measured in the far field at $x = 106D = 634$ mm. (The measurement has been done at every 10°.) In this figure, the root-mean-square error of the average curve at each time point is plotted by light solid lines. (The pressure amplitude $\Delta p$ in the figure is used later in figure 16.) The directivity is clearly seen by the polar plot of figure 9, in which radial length from the origin represents magnitude of pressure with linear scale. This shows the instantaneous directivity plot at $t = 1146$ μs, in which the experimental points ○ and ● denote positive and negative values respectively.

In view of the theoretical directivity $\sin\frac{1}{2}\theta$ for $\phi = 90°$, we assume that the observed pressure $p(\theta, t)$ is expanded in the series form

$$p(\theta, t) = b_0(t) + \sum_{k=1}^{N} b_k(t) \cos\tfrac{1}{2}k\theta + \sum_{k=1}^{N} a_k(t) \sin\tfrac{1}{2}k\theta. \tag{5.1}$$

The decomposition calculated with the least-square method for $N = 4$ gives the curves $a_k(t)$ and $b_k(t)$ illustrated in figure 10. It is seen that $a_1(t) \sin\frac{1}{2}\theta$ is a dominant component, and the others (including those coefficients not shown, omitted because of similar behaviour) are very small. This feature is consistent with the theory. The solid curve in figure 9 corresponds to $a_1(t) \sin\frac{1}{2}\theta$ at $t = 1146$ μs. For different values of $L$, we obtain similar distributions. Figures 11 and 12 illustrate the

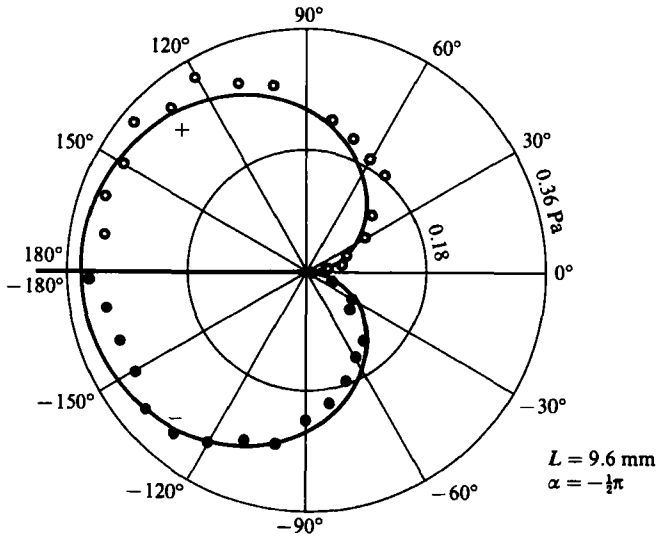


FIGURE 9. Directivity plot of the pressure. The radial distance represents magnitude of pressure in Pa. The open (positive) and filled (negative) circles show the data corresponding to figure 8 at $t = 1146$ μs, and the solid curve is $a_1(t) \sin\frac{1}{2}\theta$ with $a_1$ taken from figure 10 at the same time.

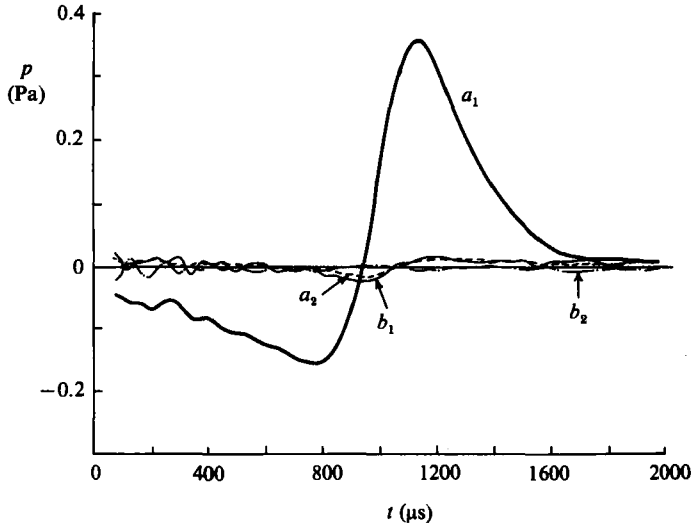


FIGURE 10. Fourier coefficients corresponding to the data of figure 8, calculated for $N = 4$. The coefficients $(b_0, b_3, b_4, a_3, a_4)$ show small fluctuation behaviours similar to those $(b_1, b_2, a_2)$ illustrated here.

Fourier coefficients and the directivity plot respectively, for a larger $L = 13.2$ mm ($U = 29.0$ m/s, $x = 630$ mm, $\phi = 90°$).

Next we consider the $\phi$-dependence. Figure 13 shows the average profiles of the pressure observed at every 30° angular position of $\phi$ from 10° in the planes $\theta = 90°$ and $-90°$, which includes the line $ON$ parallel to the nozzle, for the case $U = 30.1$ m/s and $L = 11$ mm. The data acquisition has been made at every 10°. In view of the theoretical distribution of the form $(\sin\phi)^{\frac{1}{2}}$, we sought the best-fitted curve $c(t)\,(\sin\phi)^{\frac{1}{2}}$ by the least-square method. The coefficient curve $c(t)$ is shown in figure 14. The polar

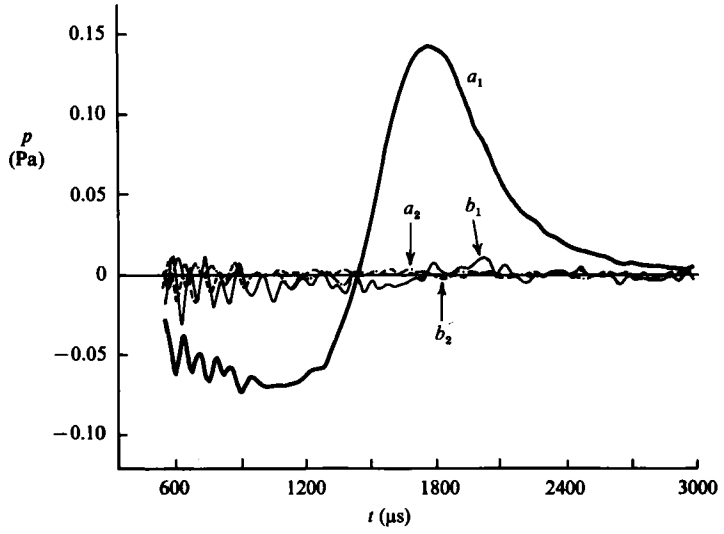


FIGURE 11. Fourier coefficients of the pressure ($x = 630$ mm, $\phi = 90°$) for the vortex path of larger $L = 13.2$ mm ($U = 29.0$ m/s, $\alpha = -\frac{1}{3}\pi$).

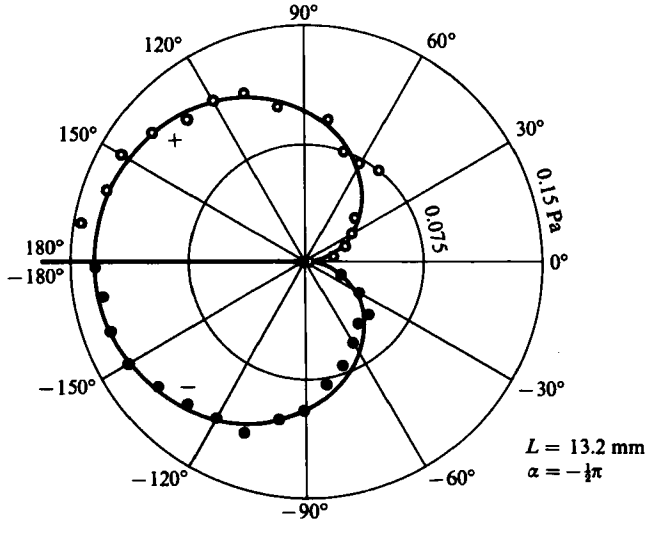


FIGURE 12. Directivity plot of the pressure for the case of figure 11 at $t = 1845$ μs. The solid curve is $a_1 \sin\frac{1}{2}\theta$, and the white and black circles are taken from average profiles.

plot of the $\phi$-directivity is given in figure 15, where the open (positive) and filled (negative) circles show experimental points and the solid curve corresponds to $c(t)\ (\sin\phi)^{\frac{1}{2}}$ at $t = 1980$ μs.

In these diagrams the theoretical directionality (3.16) is reproduced fairly well.

### 5.2. *Scaling laws*

Let us next examine the power law (3.15). From the observed profiles as shown in figure 8, we take the amplitude $\Delta p$ of pressure and plot it against the vortex speed $U$ for fixed $\theta$ and $\phi = 90°$. Figure 16 is a log–log plot of the $(\Delta p, U)$-diagram for four

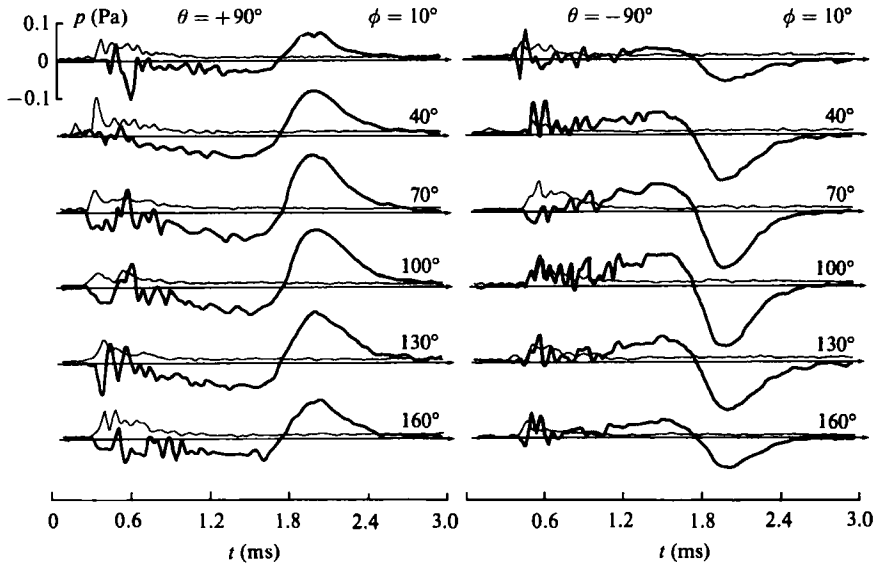


FIGURE 13. Average profiles (bold lines) of the pressure measured at six $\phi$-positions for both $\theta = \pm 90°$ ($x = 626$ mm) in the case when $U = 30.1$ m/s, $\alpha = -\frac{1}{2}\pi$ and $L = 11$ mm. The light curves denote r.m.s. error at each time point.

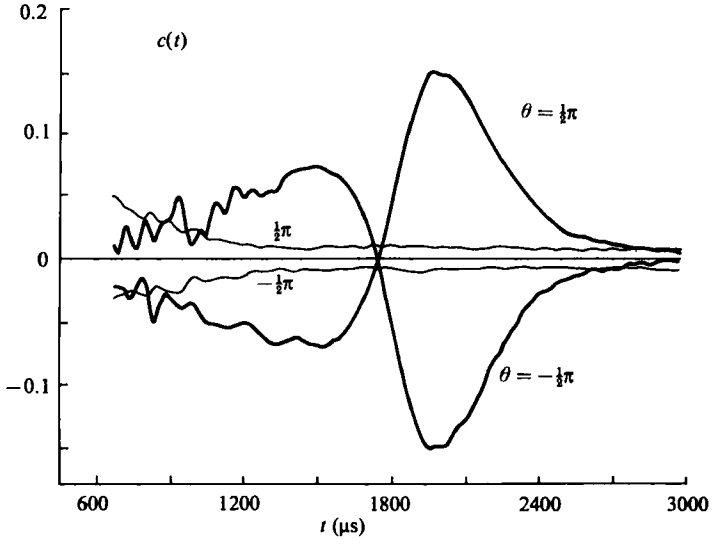


FIGURE 14. The profile $c(t)$ (corresponding to the previous figure) obtained by the least-squares method (bold), assuming that the pressure is represented by $c(t)\,(\sin\phi)^{\frac{1}{2}}$ with $\theta$ fixed. The light curves denote r.m.s. error.

values of $\theta$. The average value of the slope $\beta$ (defined in the legend) of the straight lines obtained by the least-squares method (solid lines) is found to be 2.53. This suggests the theoretical scaling law $p \propto U^{\frac{5}{2}}$ for the amplitude holds with reasonable accuracy in the experiment. In order to see this property for the whole timespan, we plot the normalized pressure $p/U^{\frac{5}{2}}$ at $\theta = -160°$ versus the normalized time $\tau = Ut/a$, for eight values of vortex speed $U$ from 31 to 61 m/s, with other parameters

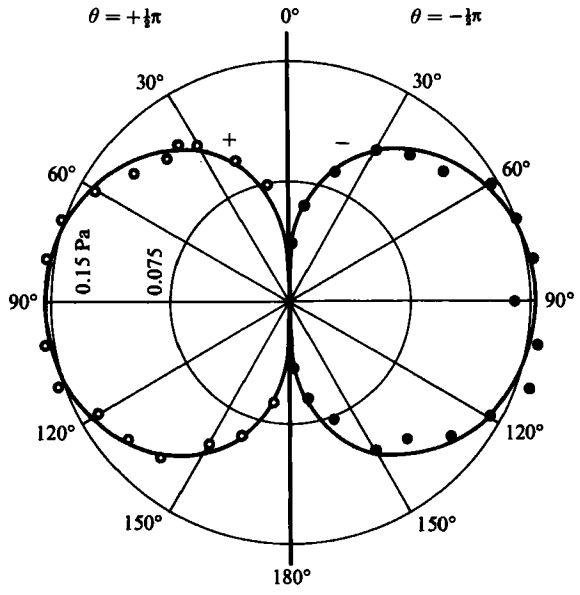


FIGURE 15. Plot of $\phi$-directivity. The solid curve is $c(t)\,(\sin\phi)^{\frac{1}{2}}$ at $t = 1980\,\mu$s, and the white (positive) and black (negative) circles show the data corresponding to figure 13 at the same time.

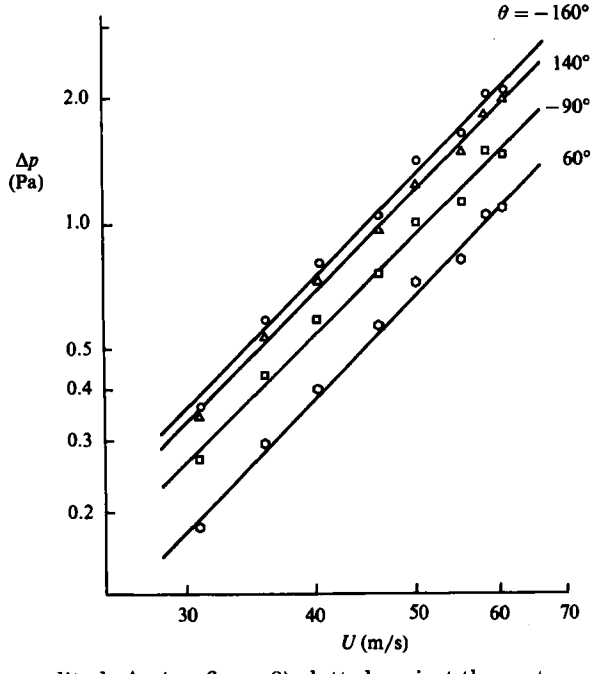


FIGURE 16. Pressure amplitude $\Delta p$ (see figure 8) plotted against the vortex speed $U$ for four values of $\theta$ ($\phi = 90°$). The straight lines are fixed by the least-square method with the assumed form $\ln \Delta p = \beta(\theta) \ln U + \gamma(\theta)$. The $x$ and $L$ are as in figure 17.

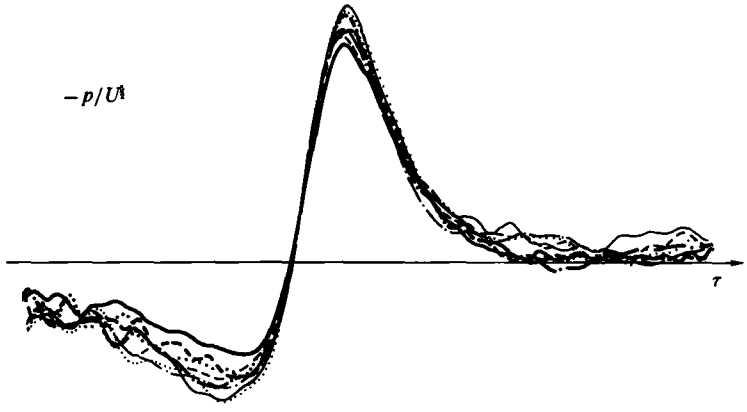


FIGURE 17. Normalized pressure $-p/U^{\frac{1}{2}}$ at $x = 628$ mm and $\theta = -160°$ ($\phi = 90°$) against normalized time $\tau = Ut/a$ ($a = 4.7$ mm, $L = 9.7$ mm) for eight values of $U$ (m/s): ——, 30.9; – – –, 35.8; ·····, 40.4; ·—·—·, 46.3; ——, 50.3; – – –, 55.7; · · · · ·, 58.7; ·—·—·, 61.0.

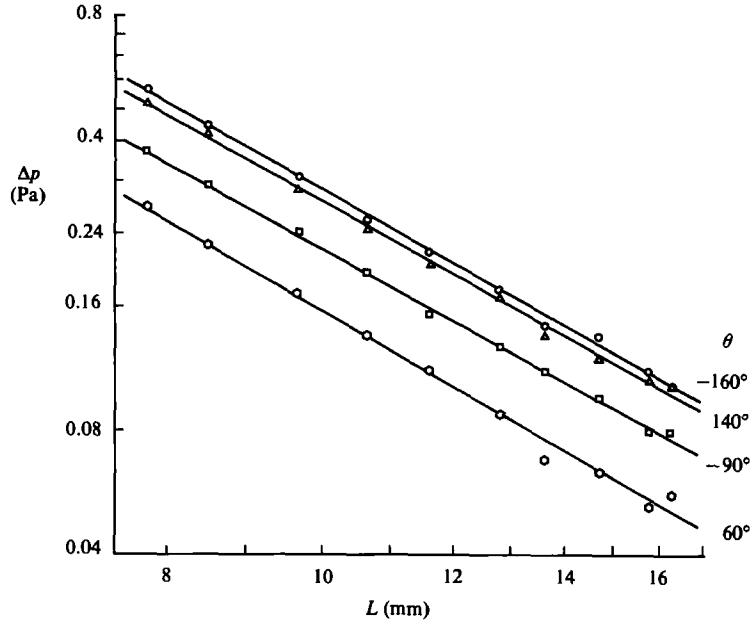


FIGURE 18. Log–log plot of $\Delta p$ against the impact distance $L$ for four values of $\theta$ ($\phi = 90°$, $x = 628$ mm, $U = 30.6$ m/s).

fixed (figure 17). In spite of the relatively large variation in magnitude of $U^{\frac{1}{2}}$, coincidence of the curves $p/U^{\frac{1}{2}}$ is reasonable. This indicates that the $U^{\frac{1}{2}}$ law of the pressure is valid in the range examined.

Figure 18 is a diagram examining the $L$-dependence, in which $\log \Delta p$ is plotted against $\log L$ for four values of $\theta$ ($\phi = 90°$) with other parameters fixed. This suggests that the experimental $L$-dependence is $p \propto L^{-2.24}$, which is not far from the theoretical law $p \propto L^{-2}$. Figure 19 shows the normalized pressure $p/L^{-2.24}$ against $\tau$ for six values of $L$ with $U = 30.6$ m/s, $x = 628$ mm and $\theta = -160°$. There are some fluctuations in the experimental values in the $(\Delta p, L)$-diagram. Hence one cannot

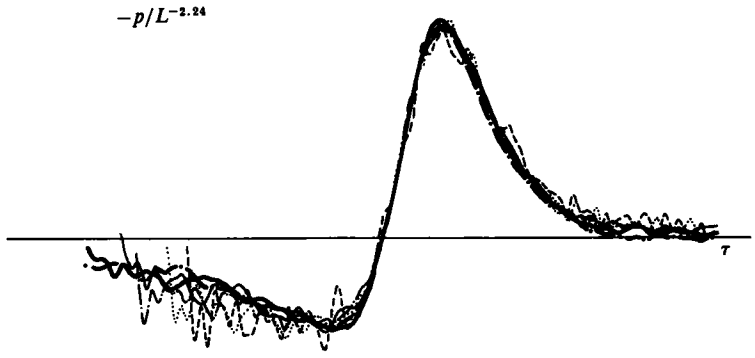


FIGURE 19. Normalized pressure $-p/L^{-2.24}$ plotted against $\tau = Ut/a$ ($U = 30.6$ m/s, $x = 628$ mm, $\theta = -160°$) for six values of $L$ (mm): ·—·—, 8.5; ——, 9.7; ——, 10.7; ·—·—, 11.6; · · · · ·, 12.8; – – –, 13.6.

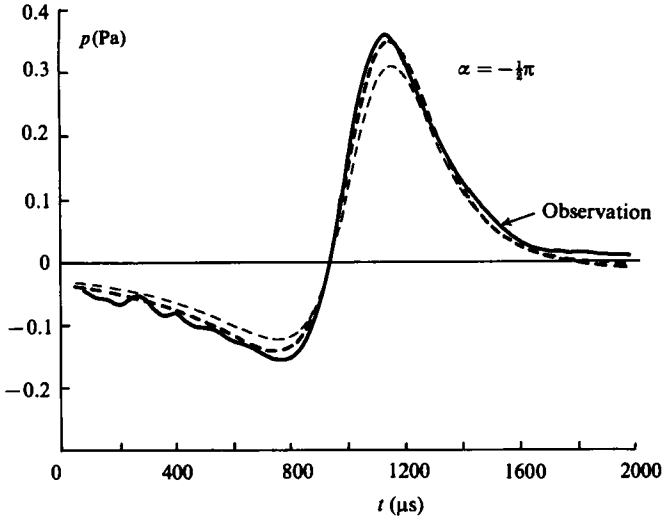


FIGURE 20. Comparison of the experimental profile $a_1(t)$ (bold line) from figure 10 with the theoretical curves for $\delta/a = 0.2$ (thin broken curve) and 0.3 (thick broken curve) for $U = 30.4$ m/s, $L = 9.6$ mm and $x = 634$ mm.

exclude the other pressure laws of the form $\Delta p \propto (L - L_0)^{-n}$, where the experimental value of $L_0$ (mm) is $-1.3$ for $n = 2.5$, 1.6 for $n = 2.0$, and 3.9 for $n = 1.5$, etc. However, it is observed that the normalization of the wave profiles by the law $p \propto L^{-2.24}$ gives a better fit than the other laws. Thus the experimental observation indicates that the predicted scaling law $p \propto U^{\frac{1}{2}}L^{-2}$ holds with reasonable accuracy.

### 5.3. *Wave profile*

The data analysis in §5.1 has shown that the wave is substantially represented by $a_1(t)\sin\frac{1}{2}\theta$ in the plane $\phi = 90°$ (with fixed $x$). Figure 20 compares the experimental profile $a_1(t)$ given in figure 10 with the theoretical curve $p/F(\theta, \phi = 90°)$ obtained by using (3.12) with the same parameters $U = 30.4$ m/s, $L = 9.6$ mm and $x = 634$ mm and using the curve of $f(t)$ for $\alpha = -\frac{1}{2}\pi$ in figure 3(*a*). The theoretical curves shown by broken curves are computed by specifying the relative core size as $\delta/a = 0.2$ (thin) and 0.3 (thick) in (3.14). It is observed that the present theory can predict the main

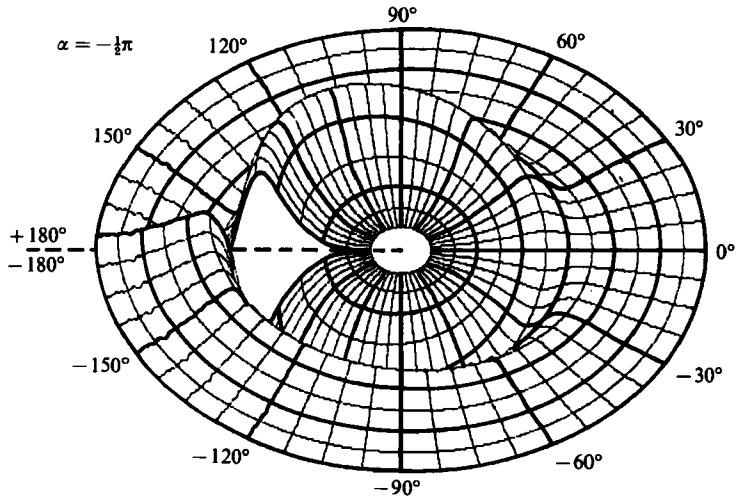


FIGURE 21. Perspective profile of the wave $a_1(t)\sin\frac{1}{2}\theta$ with $a_1(t)$ from figure 10. The radial coordinate is the time and the vertical axis the pressure. The bold line time marks are 0, 300, 600, 900, 1200 and 1500 μs from the outermost circle to the inner ones.

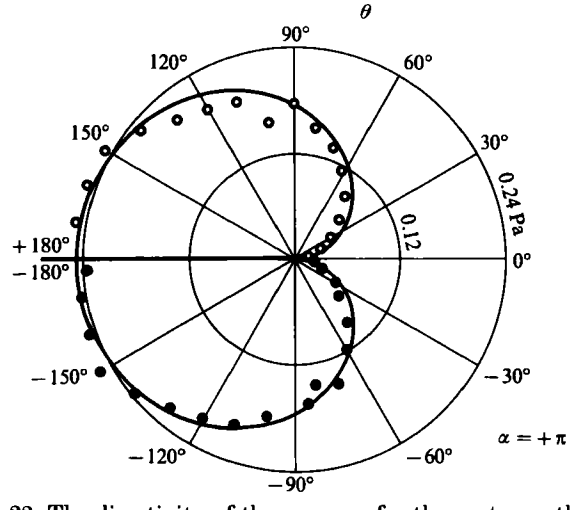


FIGURE 22. The directivity of the pressure for the vortex path with $\alpha = +\pi$, $U = 30.2$ m/s, $L = 9.9$ mm, $x = 624$ mm and $\phi = 90°$.

features of the observed profile. This verifies that the wave profile is determined by the $\frac{3}{2}$th time derivative of the volume flux of hypothetical potential flow through the vortex. Figure 21 illustrates a perspective profile of the wave $a_1(t)\sin\frac{1}{2}\theta$ with $a_1(t)$ of figure 10, the radial axis being the time and the vertical axis the pressure. The outer circles are earlier in time than the inner ones. The wave pressure takes opposite signs on both sides of the plate at $\theta/G = \pm 180°$.

## 6. Vortex motion with $\alpha = \pm\pi$

The present formula (3.12) was also examined for the vortex in the path with $\alpha = \pm\pi$ (figure 2). In this case the vortex moves parallel to the half-plane, and the vortex core impinges on the edge when $L \lesssim a$. Only the $\theta$-dependence is considered. Figures 22 and 23 show the directivity plot and the Fourier coefficients $a_k(t)$ and $b_k(t)$

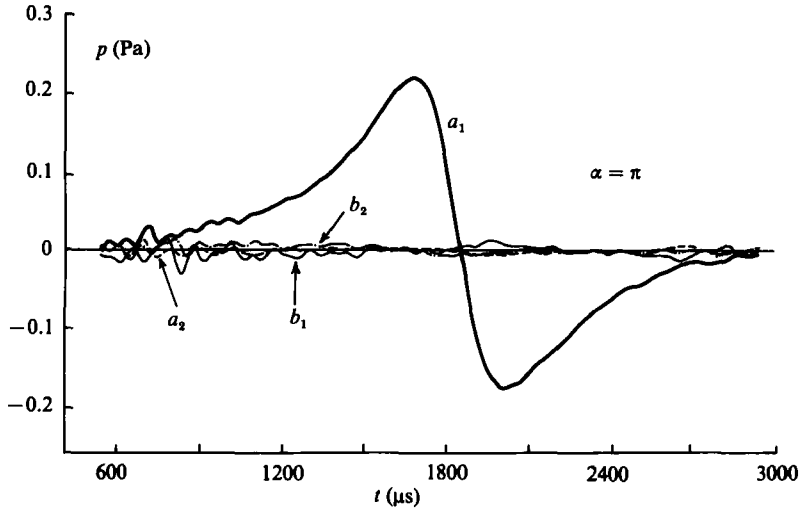


FIGURE 23. Fourier coefficients corresponding to the data of figure 22, calculated for $N = 4$ in (5.1).

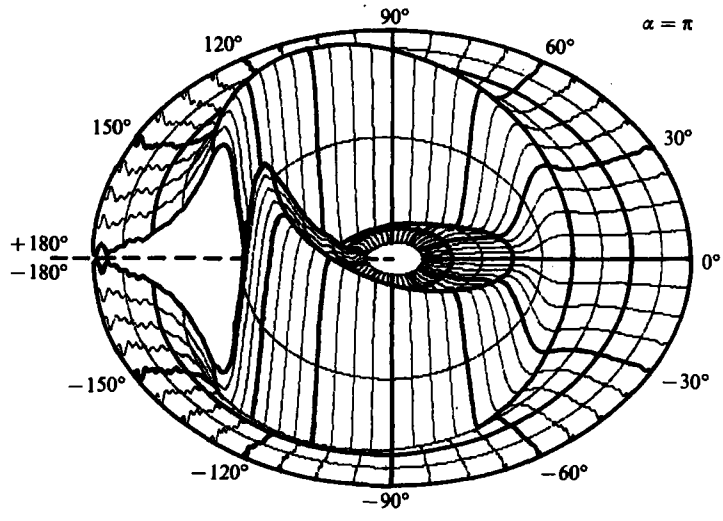


FIGURE 24. Perspective profile of the wave $a_1(t)\sin\frac{1}{2}\theta$ with $a_1(t)$ from figure 23. The bold circumferential time-mark lines are 600, 1080, 1560, 2040 and 2520 μs from the outermost circle to the inner ones.

respectively, for $\alpha = +\pi$ with $U = 30.2$ m/s, $L = 9.9$ mm and $x = 624$ mm. Here again the component $a_1$ is dominant. Figure 24 illustrates a perspective profile of the wave $a_1(t)\sin\frac{1}{2}\theta$ with $a_1(t)$ of figure 23. For the vortex running on the opposite side of the plate, where the path is defined by $\alpha = -\pi$, $U = 30.3$ m/s, $L = 10.7$ mm and $x = 622$ mm, we also examined the $\theta$-dependence of the wave, and sought the best-fitted curve $a_1(t)\sin\frac{1}{2}\theta$ by the least-square method. The coefficient $a_1(t)$ (bold solid) is shown in figure 25, together with the root-mean-square error (light solid). The perspective profile of the wave $a_1(t)\sin\frac{1}{2}\theta$ is illustrated in figure 26. Finally figure 27 compares the experimental $a_1$ curves with corresponding theoretical curves for the assumed value of the core size $\delta/a = 0.2$ (thin broken) and 0.3 (thick broken). These again confirm the validity of the formula (3.12) with reasonable accuracy.

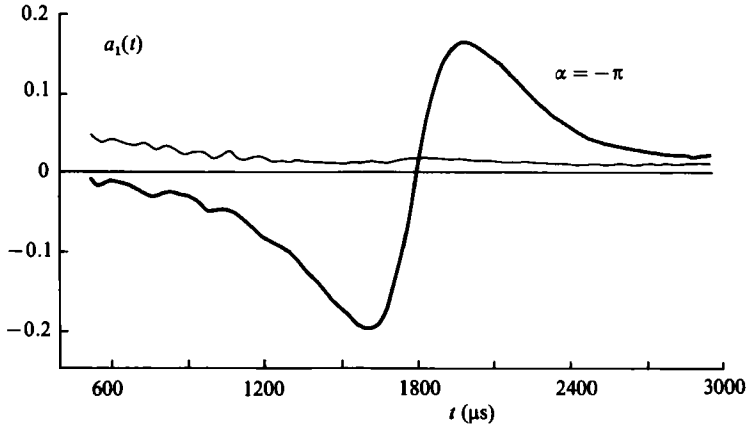


FIGURE 25. The profile $a_1(t)$ (bold) obtained for the vortex path with $\alpha = -\pi$, $L = 10.7$ mm and $U = 30.3$ m/s, assuming that the pressure (at $x = 622$ mm and $\phi = 90°$) is represented by $a_1(t)\sin\frac{1}{2}\theta$. The light curve is r.m.s. error.

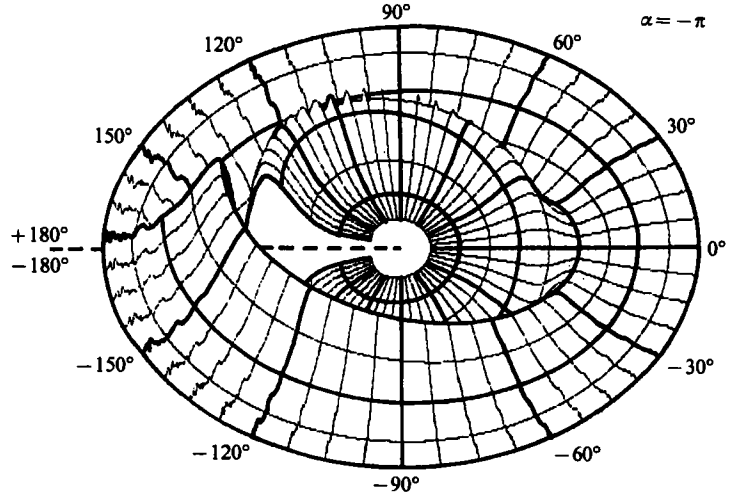


FIGURE 26. Perspective profile of the wave $a_1(t)\sin\frac{1}{2}\theta$ obtained from figure 25. The time marks are as in figure 24.

## 7. Discussion and conclusion

Acoustic emission by vortex–edge interaction is considered both theoretically and experimentally. The theory of vortex sound enables us to represent the acoustic pressure in the far field in terms of the motion of a vortex ring near the half-plane edge. The pressure is proportional to the angular factor $F(\theta, \phi)$ and the time factor $f(t)$. The directivity pattern of the intensity is represented by the cardioid curve on the equidistant points with fixed angle $\phi$. The angular dependence is the same as that of a turbulent eddy in the vicinity of a half-plane, investigated by Ffowcs Williams & Hall (1970) and Crighton & Leppington (1970).

The observed wave profiles compared well with our theoretical ones which depend on the rate of change of volume flux, $D_t^{\frac{1}{2}}[\pi a^2 v_n]$, of a hypothetical potential flow around

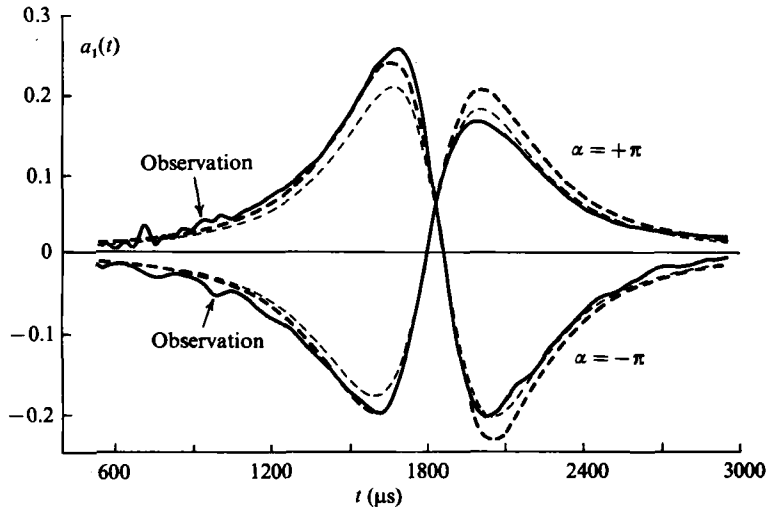


FIGURE 27. Comparison of the experimental curve $a_1(t)$ (solid) taken from figures 23 and 25 with the theoretical ones for $\delta/a = 0.2$ (thin broken curve) and 0.3 (thick broken).

the edge. This law of the temporal profile is a three-dimensional generalization of the two-dimensional problem, in which wave profile is determined by the rate at which a vortex filament traverses the streamlines of the same potential flow (Howe 1975).

The present formula predicts the scaling law $p \propto U^{\frac{5}{2}}L^{-2}$ for the sound emitted by a vortex ring of velocity $U$ and nearest distance $L$ to the edge. Owing to this property, the sound intensity is proportional to $U^5$, as was shown by Ffowcs Williams & Hall. However the $L$-dependence is different from their law $p \propto L^{-\frac{3}{2}}$. This is attributed to the different timescales of the source flow in each case.

The angular dependence and the scaling law of the pressure have been reproduced with good accuracy in the observation. In the experiment, however, the powers of $U$ and $L$ are found to be 2.53 and $-2.24$ respectively. Since the experimental values are scattered in the $p$–$L$ diagram, we cannot exclude the other power laws $p \propto (L-L_0)^{-n}$.

One of the important results of the present work is the agreement between the predicted wave profile and the observed one, as shown in figures 20 and 27. This verifies that the profile is determined by the $\frac{3}{2}$th time derivative of the volume flux (through the vortex ring) of a hypothetical potential flow around the edge. In order to calculate the wave profile we used two simplifying assumptions, in addition to the basic assumptions of the theory in §2.1. First, the vortex is supposed to take a straight path. This is equivalent to the application of a force that will give rise to emission of a dipole wave. However, the analysis in Appendix B shows that this correction is very small. Secondly the vortex ring is assumed to have a vortex core of the size $\delta/a = 0.2$ to 0.3 and to satisfy the relation (3.14).

Finally, it should be noted that the velocity of the potential flow around the edge becomes infinite at the edge where viscous effect may not be neglected. In an investigation of sound diffraction by a half-plane in a viscous medium at rest, Alblas (1957) showed that small viscosity removes the singularity in the velocity at the edge without appreciably affecting the far-field pressure. In a different point of view to avoid the singularity, Jones (1972) considered the effect of a Kutta condition at the

edge and showed that in some circumstances that condition alters the $U^5$ law of intensity to a $U^3$ law. It is shown that observation does not support this. It appears that the present experiment without mean flow supports the Alblas' idea of the viscosity effect removing the singularity at the edge without affecting the far-field pressure appreciably.

The authors would like to express their deep appreciation to Professor T. Murakami in Kyushu University, where the present experimental work has been done with his kind cooperation. They are also grateful to the editor and the referees for comments that led to a clearer presentation of this work.

## Appendix A. Low-frequency Green function

The diffraction problem is well-formulated with a Fourier representation $\hat{G}$ of the Green function $G$:

$$G(\boldsymbol{x},\boldsymbol{y};t)=\frac{1}{2\pi}\int_{-\infty}^{\infty}\hat{G}\left(\boldsymbol{x},\boldsymbol{y};\frac{\omega}{c}\right)\mathrm{e}^{-\mathrm{i}\omega t}\,\mathrm{d}\omega. \tag{A 1}$$

Then (2.6) is reduced to

$$(\nabla^2+k^2)\,\hat{G}(\boldsymbol{x},\boldsymbol{y};k)=-\delta(\boldsymbol{x}-\boldsymbol{y}), \tag{A 2}$$

where $k=\omega/c$, and the boundary condition is

$$\partial\hat{G}/\partial n=0 \quad \text{on } S. \tag{A 3}$$

The solution of this problem was given exactly by Macdonald (1915) and used by Ffowcs Williams & Hall (1970) and Crighton & Leppington (1970). The solution is also found by using the Wiener–Hopf method (Noble 1958).

We summarize their results briefly and then present a series-form solution for small $kl$. The incident field is

$$\hat{G}_0(\boldsymbol{x},\boldsymbol{y};k)=\frac{1}{4\pi|\boldsymbol{x}-\boldsymbol{y}|}\mathrm{e}^{\mathrm{i}k|\boldsymbol{x}-\boldsymbol{y}|}, \tag{A 4}$$

where the time dependence of the field is proportional to $\mathrm{e}^{-\mathrm{i}\omega t}$. Since $|\boldsymbol{x}|=x$ is assumed to be sufficiently large compared with $|\boldsymbol{y}|=y$, this is expressed asymptotically as

$$\hat{G}_0(\boldsymbol{x},\boldsymbol{y};k)=A\exp[-\mathrm{i}k(\hat{x}_1y_1+\hat{x}_2y_2)], \tag{A 5}$$

where

$$A=\frac{1}{4\pi x}\exp[\mathrm{i}kx-\mathrm{i}k\hat{x}_3y_3], \quad \hat{\boldsymbol{x}}=\boldsymbol{x}/x=(\hat{x}_1,\hat{x}_2,\hat{x}_3). \tag{A 6}$$

The unit vector $\hat{\boldsymbol{x}}$ is given another form by using the polar angle $\phi$ and the azimuthal angle $\theta$:

$$\hat{x}_1=\sin\phi\cos\theta, \quad \hat{x}_2=\sin\phi\sin\theta, \quad \hat{x}_3=\cos\phi. \tag{A 7}$$

The problem (A 2) and (A 3) is reduced to the problem of finding a scattered field $\hat{G}_s(\boldsymbol{x},\boldsymbol{y};k)$ associated with the incident field $\hat{G}_0(\boldsymbol{x},\boldsymbol{y};k)$, where the total Green function $\hat{G}$ is given by $\hat{G}_0+\hat{G}_s$. This is accomplished by the Wiener–Hopf technique, and the scattered field $\hat{G}_s$ is given by

$$\hat{G}_s=-\frac{\mathrm{i}}{\pi^{\frac{1}{2}}}A\,\mathrm{e}^{\frac{1}{4}\mathrm{i}\pi}[-F(v_1)\,\mathrm{e}^{-\mathrm{i}KY\cos(\Theta-\theta)}+F(v_2)\,\mathrm{e}^{-\mathrm{i}KY\cos(\Theta+\theta)}] \tag{A 8}$$

(Noble 1958, chap. II), where

$$F(v) = \int_v^\infty \mathrm{e}^{\mathrm{i}u^2}\,\mathrm{d}u \quad \text{(Fresnel function)}, \tag{A 9}$$

$$\left.\begin{aligned} v_1 = (2KY)^{\frac{1}{2}}\cos\tfrac{1}{2}(\Theta-\theta), \quad v_2 = (2KY)^{\frac{1}{2}}\cos\tfrac{1}{2}(\Theta+\theta), \\ K = k(1-\hat{x}_3^2)^{\frac{1}{2}} = k\sin\phi, \\ Y = (y_1^2+y_2^2)^{\frac{1}{2}}, \quad \Theta = \tan^{-1}\left(\frac{y_2}{y_1}\right). \end{aligned}\right\} \tag{A 10}$$

The expressions (A 4) and (A 8) give the total Green function.

The compactness conditions (ii) and (iii) enable us to use the low-frequency Green function (Howe 1975), which is expressed by first few terms of the asymptotic expansion valid for small $kl$. Owing to the relation $K = k\sin\phi$ along with the order estimations like $Y = O(l)$, the parameter $KY = O(\epsilon)$ is regarded as small. Hence the expressions (A 4) and (A 8) can be developed into the asymptotic series

$$\hat{G}_0 = \frac{1}{4\pi x}\mathrm{e}^{\mathrm{i}kx}\left(1-\mathrm{i}k\frac{\boldsymbol{x}\cdot\boldsymbol{y}}{x}+(\mathrm{i}k)^2\frac{(\boldsymbol{x}\cdot\boldsymbol{y})^2}{2x^2}+\ldots\right), \tag{A 11}$$

$$\hat{G}_{\mathrm{S}} = \hat{G}_{\frac{1}{2}}+\hat{G}_1+\hat{G}_{\frac{3}{2}}+\hat{G}_2+\ldots, \tag{A 12}$$

$$\left.\begin{aligned} &\hat{G}_m = F_m(\boldsymbol{X},\boldsymbol{Y},x_3)\,(-\mathrm{i}k)^m\exp(\mathrm{i}kx-\mathrm{i}k\cos\phi\; y_3), \\ &F_m = A_m\,\Phi_m(\boldsymbol{X})\,\Phi_m(\boldsymbol{Y})\,x^{-m-1} \quad (m=\tfrac{1}{2},1,\tfrac{3}{2},2,\ldots), \\ &A_{\frac{1}{2}} = \frac{1}{(2\pi^3)^{\frac{1}{2}}}, \quad A_1 = -\frac{1}{4\pi}, \quad A_{\frac{3}{2}} = \frac{1}{6}\left(\frac{2}{\pi^3}\right)^{\frac{1}{2}}, \quad A_2 = -\frac{1}{16\pi}, \quad \ldots \end{aligned}\right\} \tag{A 13}$$

$$\Phi_m(\boldsymbol{X}) = (x\sin\phi)^m\sin m\theta, \quad \Phi_m(\boldsymbol{Y}) = Y^m\sin m\Theta, \tag{A 14}$$

$$\boldsymbol{X} = (x_1,x_2), \quad \boldsymbol{Y} = (y_1,y_2). \tag{A 15}$$

It is readily seen that the condition $\partial(\hat{G}_0+\hat{G}_{\mathrm{S}})/\partial y_2 = 0$, on $y_2 = 0$ and $-\infty < y_1 < 0$, is satisfied with the above expressions. The functions $\Phi_m$ are harmonic functions, and, in particular, $\Phi_{\frac{1}{2}}$ represents the velocity potential of the flow around the edge of the half-plane.

## Appendix B. Influence of the half-plane on the vortex motion

The perturbation velocity by the half-plane (semi-infinite plate) is estimated here when the vortex path is sufficiently distant from the edge. This is accomplished by using the velocity potential of a simple source satisfying the condition of vanishing normal velocity at the boundary, given by Macdonald (1915). The potential of a unit strength source is denoted by $\Phi_{\mathrm{S}}(R,\theta,z;\,R_0,\theta_0,z_0=0)$, where $(R,\theta,z)$ is the cylindrical coordinate and the variables with suffix 0 stand for the source position situated in the equatorial plane $z_0 = 0$. Based on the property that the velocity field of a vortex ring tends to that of a dipole asymptotically at large distances, the influence from the edge is calculated by using the dipole potential $\Phi_{\mathrm{D}}$ derived from $\Phi_{\mathrm{S}}$ as

$$\Phi_{\mathrm{D}} = P\left(e_R\frac{\partial}{\partial R_0}+e_\theta\frac{1}{R_0}\frac{\partial}{\partial\theta_0}\right)\Phi_{\mathrm{S}},$$

where $\boldsymbol{e} = (e_R, e_\theta, 0)$ is the unit vector in the direction of the dipole axis coinciding with the axis of the vortex ring and $P$ denotes the dipole strength. Corresponding

to the vortex ring of radius $a$ and strength $\Gamma$, the dipole strength is given by $P = \pi a^2 \Gamma$.

Macdonald's expression for the source potential of a unit rate of outflow takes the form

$$\Phi_S = -\frac{1}{4\pi r}\left(\frac{1}{2}+\frac{2}{\pi}\tan^{-1}(\tanh\tfrac{1}{2}\xi)\right)-\frac{1}{4\pi r'}\left(\frac{1}{2}+\frac{2}{\pi}\tan^{-1}(\tanh\tfrac{1}{2}\xi')\right), \tag{B 1}$$

where

$$r^2 = R^2+R_0^2-2RR_0\cos(\theta-\theta_0)+z^2,$$

$$r'^2 = R^2+R_0^2-2RR_0\cos(\theta+\theta_0)+z^2,$$

$$\sinh\xi = \frac{2}{r}(RR_0)^{\frac{1}{2}}\cos\tfrac{1}{2}(\theta-\theta_0),$$

$$\sinh\xi' = -\frac{2}{r'}(RR_0)^{\frac{1}{2}}\cos\tfrac{1}{2}(\theta+\theta_0).$$

In order to get an estimate of the influence of the plate, we are particularly interested in the perturbation velocity when the vortex is at the position $\theta = 0$. Some straightforward calculations show

$$\left.\begin{aligned}\frac{\partial}{\partial R_0}\Phi_S &= -\frac{1}{4\pi}\frac{\partial}{\partial R_0}\frac{1}{r},\\ \frac{1}{R_0}\frac{\partial}{\partial\theta_0}\Phi_S &= -\frac{1}{4\pi}\frac{1}{R_0}\frac{\partial}{\partial\theta_0}\frac{1}{r}-\frac{1}{48\pi^2}\frac{\theta}{R_0^2}+O(\theta^2, R'\theta),\end{aligned}\right\} \tag{B 2}$$

where $|\theta| \ll 1$, $\theta_0 = 0$, $R' = R-R_0$ and $|R'| \ll R_0$. The first terms on the right-hand sides of (B 2) represent the dipole potential velocity in an unbounded domain and the remaining terms are the perturbations from the plate. Let us consider the vortex moving perpendicularly to the plate and passing by the edge at a distance $L(=R_0)$ when $\theta_0 = 0$. Hence we put $e_R = 0$ and $e_\theta = 1$. The perturbation velocity $(u', v', 0)$ brought about by the plate is given by

$$\left.\begin{aligned}v' &= \frac{1}{R}\frac{\partial}{\partial\theta}\left(\Phi_D+\frac{1}{4\pi R_0}\frac{\partial}{\partial\theta_0}\frac{1}{r}\right)\Big|_{R=R_0,\,\theta=0,\,(R_0=L)}\\ &= -\frac{P}{48\pi^2}\frac{1}{L^3} = -\frac{\Gamma}{48\pi a}\frac{a^3}{L^3}\end{aligned}\right\} \tag{B 3}$$

and $u' = 0$. Using the formula (3.14) for the vortex velocity $U$, and writing $v = |v'|$, we obtain

$$\frac{v}{U} = \frac{1}{12B}\left(\frac{a}{L}\right)^3. \tag{B 4}$$

Thus it is found that the perturbation diminishes like $(a/L)^3$ as the distance $L$ increases. For the case of the relative core size $\delta/a = 0.2$–$0.3$, the factor $B$ takes the values 3.4–3.0. When the distance $L$ is $2a$, or $3a$, as in the experiment, the fractional ratio of the perturbation velocity (B 4) takes very small values, that is

$$v/U = 3.5\times10^{-3} \quad \text{or } 1.0\times10^{-3} \tag{B 5}$$

respectively, with $B = 3.0$.

Suppose that the vortex path was made straight by a fictitious force $F(t)$ that was applied to the vortex. The force is estimated in order of magnitude as

$F_0 = \rho_0 P(v/U)/\tau$, where $\tau = L/U$ is the timescale of the vortex motion. This force causes emission of a dipole wave. Its amplitude would have a magnitude of order

$$P_D = \frac{1}{c}\frac{dF}{dt}\frac{1}{x}$$

(Curle 1955). We may approximate $dF/dt$ by $F_0/\tau$. Thus we obtain the relative magnitude of $P_D$ to $P_*$ of (3.13) in the main text, which expresses the magnitude of the edge sound under consideration, as

$$\frac{P_D}{P_*} = \frac{1}{c}\frac{F_0}{\tau}\frac{1}{x}\Big/\rho_0 \frac{U^{\frac{3}{2}}\Gamma}{c^{\frac{1}{2}}}\frac{a^2}{L^2}\frac{1}{x} = \frac{v}{U}\left(\frac{U}{c}\right)^{\frac{1}{2}}.$$

Considering the estimated value of $v/U$ in (B 5) and the smallness of the Mach number $U/c$, we find that the dipole-wave correction would be very small.

## REFERENCES


Alblas, J. B. 1957 *Appl. Sci. Res.* **6A**, 237–262.

Cannell, P. A. & Ffowcs Williams, J. E. 1973 *J. Fluid Mech.* **58**, 65–80.

Crighton, D. G. 1972 *J. Fluid Mech.* **51**, 357–362.

Crighton, D. G. & Leppington, F. G. 1970 *J. Fluid Mech.* **43**, 721–736.

Curle, N. 1955 *Proc. R. Soc. Lond.* A **231**, 505–514.

Ffowcs Williams, J. E. & Hall, L. H. 1970 *J. Fluid Mech.* **40**, 657–670.

Goldstein, M. E. 1976 *Aeroacoustics*. McGraw-Hill.

Howe, M. S. 1975 *J. Fluid Mech.* **71**, 625–673.

Jones, D. S. 1972 *J. Inst. Maths. Applics.* **9**, 114–122.

Kambe, T. 1984 *J. Sound Vib.* **95** (3), 351–360.

Kambe, T. & Minota, T. 1983 *Proc. R. Soc. Lond.* A **386**, 277–308.

Kambe, T. & Mya Oo, U. 1984 *J. Phys. Soc. Jpn.* **53**, 2263–2273.

Lamb, H. 1932 *Hydrodynamics*, 6th edn. Cambridge University Press.

Landau, L. D. & Lifshitz, E. M. 1959 *Fluid Mechanics*, §74. Pergamon.

Lighthill, M. J. 1952 *Proc. R. Soc. Lond.* A **211**, 564–587.

Lighthill, M. J. 1978 *Waves in Fluids*. Cambridge University Press.

Macdonald, H. M. 1915 *Proc. Lond. Math. Soc.* (2) **14**, 410–427.

Möhring, W. 1978 *J. Fluid Mech.* **85**, 685–691.

Noble, B. 1958 *Methods based on the Wiener–Hopf Technique*. Pergamon.

Obermeier, F. 1979 *Acustica* **42**, 56–61.

Obermeier, F. 1980 *J. Sound Vib.* **72**, 39–49.